





Ultraviolet to far-infrared dielectric function of *n*-doped cadmium oxide thin filmsJ. Ryan Nolen ¹, Evan L. Runnerstrom ^{2,3}, Kyle P. Kelley,² Ting S. Luk,^{4,5} Thomas G. Folland ⁶,
Angela Cleri,⁷ Jon-Paul Maria,⁷ and Joshua D. Caldwell ⁶¹*Interdisciplinary Materials Science Program, Vanderbilt University, Nashville, Tennessee, USA*²*Department of Materials Science and Engineering, North Carolina State University, Raleigh, North Carolina, USA*³*Army Research Office, CDCC US Army Research Laboratory, Research Triangle Park, North Carolina, USA*⁴*Sandia National Laboratories, Albuquerque, New Mexico, USA*⁵*Center for Integrated Nanotechnologies, Sandia National Laboratories, Albuquerque, New Mexico, USA*⁶*Department of Mechanical Engineering, Vanderbilt University, Nashville, Tennessee, USA*⁷*Department of Materials Science and Engineering, The Pennsylvania State University, University Park, Pennsylvania, USA*

(Received 26 July 2019; accepted 5 February 2020; published 28 February 2020; corrected 13 August 2020)

Spectroscopic ellipsometry and Fourier transform infrared spectroscopy were applied to extract the ultraviolet to far-infrared ($150\text{--}33333\text{ cm}^{-1}$) complex dielectric functions of high-quality, sputtered indium-doped cadmium oxide (In:CdO) thin crystalline films on MgO substrates possessing carrier densities (N_d) ranging from $1.1 \times 10^{19}\text{ cm}^{-3}$ to $4.1 \times 10^{20}\text{ cm}^{-3}$. A multiple oscillator fit model was used to identify and analyze the three major contributors to the dielectric function and their dependence on doping density: interband transitions in the visible, free-carrier excitations (Drude response) in the near- to far-infrared, and IR-active optic phonons in the far-infrared. More specifically, values pertinent to the complex dielectric function such as the optical band gap (E_g), are shown here to be dependent upon carrier density, increasing from approximately 2.5–3 eV, while the high-frequency permittivity (ϵ_∞) decreases from 5.6 to 5.1 with increasing carrier density. The plasma frequency (ω_p) scales as $\sqrt{N_d}$, resulting in ω_p values occurring within the mid- to near-IR, and the effective mass (m^*) was also observed to exhibit doping density-dependent changes, reaching a minimum of $0.11m_0$ in unintentionally doped films ($1.1 \times 10^{19}\text{ cm}^{-3}$). Good quantitative agreement with prior work on polycrystalline, higher-doped CdO films is also demonstrated, illustrating the generality of the results. The analysis presented here will aid in predictive calculations for CdO-based next-generation nanophotonic and optoelectronic devices, while also providing an underlying physical description of the key properties dictating the dielectric response in this atypical semiconductor system.

DOI: [10.1103/PhysRevMaterials.4.025202](https://doi.org/10.1103/PhysRevMaterials.4.025202)

I. INTRODUCTION

Transparent conducting oxides (TCOs) are most commonly utilized in applications requiring high optical transmittance and low electrical resistivity. This unique combination of optoelectronic properties is achieved by semiconductor materials possessing visible to ultraviolet band gaps and high defect and/or extrinsic dopant concentrations, with the associated impurity close to the conduction band edge [1,2]. In recent years, TCOs have also found utility as potential alternative plasmonic materials for nanophotonic applications within the near (NIR) to midinfrared (MIR), due to the lower optical losses in reference to gold and most doped semiconductors in this spectral range [3,4].

Although cadmium oxide (CdO) has been known as a TCO for over a century [5], recent work has demonstrated *n*-doped CdO as a unique plasmonic material with broad spectral tunability and exceptionally low optical losses, surpassed only by graphene [3]. These properties are due to the low effective mass (m^* ranging from 0.12–0.26 in epitaxially grown films with carrier densities ranging from $N_d \approx 10^{19}$ – 10^{20} cm^{-3} , and high electron mobility ($\mu > 300\text{ cm}^2/\text{V-s}$ between $N_d \approx 10^{19}$ – 10^{21} cm^{-3}) [3]. Interestingly, it has been demonstrated that μ actually increases with increasing carrier density over a broad range of accessible doping levels,

reaching a maximum value of almost $500\text{ cm}^2/\text{Vs}$ at $N_d \approx 5 \times 10^{19}\text{ cm}^{-3}$ [3]. Multiple aliovalent dopants have been employed to exhibit this novel behavior including Dy^{3+} [3], In^{3+} [6], Y^{3+} [7], and F^- [8], each of which have atomic radii similar in size to either Cd^{2+} or O^{2-} . This allows for substitutional, aliovalent cation (e.g., Dy^{3+} for Cd^{2+}) or anion (e.g., F^- for O^{2-}) doping while minimizing lattice strain, and thus, carrier scattering. Very high-quality CdO film growth has recently been demonstrated using high-power impulse magnetron sputtering (HiPIMS) [7]. This technique uses a pulsed (1–10 μs short pulses) dc plasma in order to attain extremely large power densities ($\geq \text{kW}/\text{cm}^2$) and therefore high sputter rates and high-density films, all while maintaining low surface roughness [9,10]. Surprisingly, HiPIMS deposition offers comparable doping precision, carrier mobility, and even improved material quality in comparison to CdO grown via molecular beam epitaxy (MBE), while allowing for potential scalability.

While traditional approaches for plasmonic applications in the near-IR have utilized noble metals, with applications realized in surface plasmon resonance (SPR) biosensing [11–13], enhanced vibrational spectroscopies such as surface enhanced Raman scattering (SERS) [14–16], surface enhanced infrared absorption (SEIRA) [17–19], and optical metasurfaces such as

planar lenses [20–22], there are significant drawbacks to using metals for MIR plasmonics [23]. First, metals have large, fixed carrier densities resulting in static plasma frequencies that fall within the visible to ultraviolet regime, complicating their applications to longer wavelengths. Further, fast electron-electron scattering at these large carrier densities brings about high Drude losses, which are exacerbated in the MIR. These losses, combined with extremely large negative permittivity values in this spectral range, render noble metals impractical for applications requiring narrow resonant features such as chemical sensing [24] or narrow-band IR sources [25]. In contrast, CdO films are capable of supporting relatively sharp (Q factors calculated here from the dielectric function to be as high as 24, five to ten times larger than gold in the MIR [26,27]), frequency tunable resonances in the MIR, including highly absorptive surface-plasmon-polariton (SPP) and epsilon-near-zero (ENZ) modes, all without the need for nanostructuring [8]. ENZ polaritons can be induced near the frequency at which $Re(\epsilon) \rightarrow 0$ in polaritonic films that are significantly thinner than the free-space wavelength at the plasma frequency ($t \approx \lambda_p/50$, which is less than ~ 100 nm in CdO films at MIR frequencies) [28,29]. These modes result from the strong coupling between polaritons supported on the opposing interfaces of the thin film, which hybridize into high- and low-frequency branches, with the former corresponding to the aforementioned ENZ behavior. Careful *in situ* control over N_d during film growth has opened the door to monolithic, multilayered films that exhibit metamaterial-like optical properties such as multifrequency thermal emission [30]. Similar multilayer films have also been used to demonstrate the potential for strongly coupled polaritonic systems, as recently demonstrated by our groups [31,32].

Before CdO can be adopted for advanced applications, it is imperative that an accurate dielectric function be established and a full understanding of the various contributions controlling this function. This is especially pertinent for CdO, as the carrier density-driven modifications of the band gap, effective mass and high-frequency permittivity ensure that the dielectric function employed must be extracted from a film with similar doping levels, unless appropriate trends can be identified. While prior work examined the NIR dielectric function of nonepitaxial, polycrystalline CdO films [33], accurate experimental MIR dielectric functions for high quality/high mobility (i.e., grown by MBE or HiPIMS), CdO films have yet to be reported. Here, we experimentally measure the UV to far-IR (FIR) optical properties of epitaxial In:CdO thin films on MgO substrates (grown via HiPIMS) as a function of free-carrier density ($1.1 \times 10^{19} \text{ cm}^{-3}$ – $4.1 \times 10^{20} \text{ cm}^{-3}$) and extract their corresponding dielectric functions. We utilize both visible (V-VASE) and IR variable angle spectroscopic ellipsometry (IR-VASE) to measure the optical response and utilize these measurements to extract the complex dielectric function. Through this effort, we extend the focus beyond the NIR to include the ultraviolet and visible as well as the mid-to far-IR, thereby accommodating the optical properties within the various IR atmospheric windows. In past work, high carrier densities ($N_d > 5 \times 10^{20} \text{ cm}^{-3}$) were achieved by using dopant densities as high as 10 mol%, potentially leading to the formation of secondary phases [34]. In comparison, the carrier

densities of the films in this study remain below the dopant solubility limit. All films are epitaxial, phase pure, with consistently narrow x-ray line widths and low surface roughness values [3,7,8]. In addition to extracting the complex dielectric functions, we also compare the optical properties of these high-quality, In:CdO films with values reported in past work for polycrystalline, nonepitaxial In:CdO films. To supplement visible and IR-VASE measurements, which provide ellipsometric data above 333 cm^{-1} , we utilize Fourier transform infrared (FTIR) spectroscopy to extend the measured range to 150 cm^{-1} , allowing us to also determine the effects of low-energy phonons on the FIR dielectric function. Combined, these techniques allow for a complete characterization of the polarization-dependent reflection and transmission coefficients, and thus the tunable carrier concentration-dependent factors comprising the dielectric response of In:CdO from the UV to the FIR.

II. DIELECTRIC FUNCTION MODELING

The IR-VASE and V-VASE techniques are powerful tools for determining the optical properties of thin films. Ellipsometry measurements relate the ratio of outgoing-parallel (p) to incident-perpendicular (s) Fresnel reflectivity coefficients to two ellipsometric parameters, ψ and Δ , through the following expression:

$$\rho = \frac{R_p}{R_s} = \tan(\psi)e^{i\Delta}. \quad (1)$$

In this expression, ψ and Δ represent the amplitude and phase difference between the two polarizations, respectively. Combined, these two quantities enable VASE as a comprehensive approach towards quantifying the optical response of films and substrates featuring isotropic and anisotropic crystal structures [35].

To extract the dielectric function of the various In:CdO films as a function of carrier density, we fit ellipsometric spectra (Fig. 1) using a multiple oscillator model in conjunction with least-squares fitting within the WVASE software (J. A. Woollam Co., Version: 3.882). Our model incorporates the dielectric function of the single-crystal MgO substrate, which we separately measured and modeled with a previously reported oscillator model [36]. Our model enables least-squares fitting within WVASE to account for the small variations in damping and phonon energies (i.e., crystal quality) that occur between different MgO substrates. The CdO film coating the MgO substrate was modeled as a bulk layer topped by a thin surface carrier depletion or accumulation layer, depending on the Fermi level of the CdO film with respect to the Fermi stabilization level (4.9 eV below vacuum) [37]. The position of the Fermi level with respect to the stabilization energy establishes the dominant native defects in a semiconductor: if the Fermi level lies below (above) this energy, charge donor (acceptor) defects will populate the surface of the CdO film, giving rise to the aforementioned charge accumulation (depletion) layer [38]. This model accounts for the spatially varying dielectric function that results from this carrier depletion/accumulation layer. A detailed report of the fitting procedure is provided in the Supplemental Material [39].

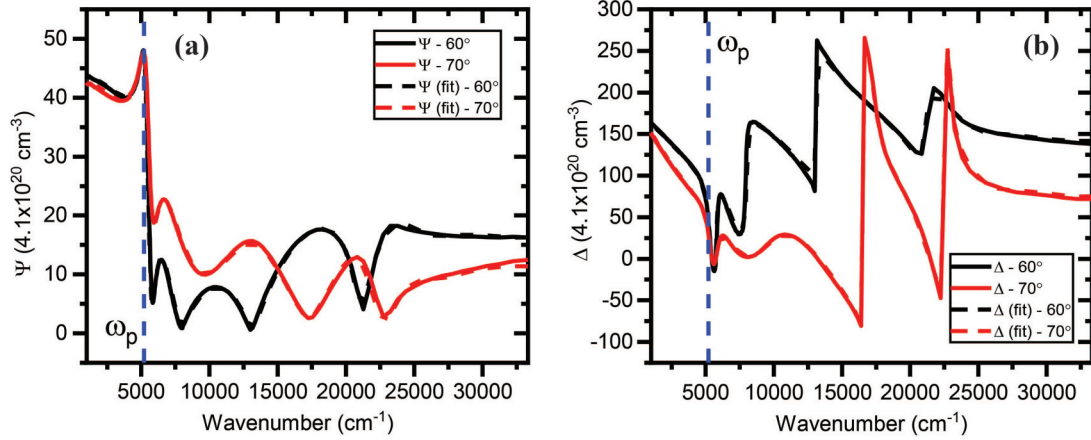


FIG. 1. Representative experimental (a) ψ and (b) Δ spectra and corresponding least-squares fits for a In:CdO film with a carrier density of $4.1 \times 10^{20} \text{ cm}^{-3}$ at 60° (black) and 70° (red) incident angles. The vertical black dotted line represents the extracted plasma frequency of the film ($\omega_p = 5,218 \text{ cm}^{-1}$).

While the film thickness can be determined from ellipsometric measurements, in order to reduce the number of free fitting parameters, we implemented x-ray reflectivity (XRR), which provides film thickness measurements with accuracy on the order of the x-ray wavelength (Cu $K\alpha$: 1.54 \AA). Room temperature carrier density and dc mobility values were collected via Hall effect measurements using the van der Pauw configuration. It is important to note that the film thicknesses were chosen such that they were significantly larger ($>150 \text{ nm}$) than the threshold for supporting ENZ polaritons [29]. This was done in order to ensure that the extracted dielectric function was representative of the bulk behavior and to avoid the additional thickness dependence of such ENZ modes upon the dielectric function, as was recently reported for tin-doped indium oxide [40].

III. EFFECTS OF FREE CARRIERS ON UV TO VISIBLE DIELECTRIC FUNCTION

Due to a direct band gap (E_g) occurring at visible frequencies and an upper limit on the ω_p (due to doping limitations) CdO possesses a broad transparency window in the visible to NIR that is bound by E_g and the ω_p . Here, we examine the absorption features associated with the direct band gap of CdO, focusing first on the impact upon the visible dielectric function and its relationship with doping levels.

The CdO dielectric function near the direct band gap can be accurately modeled using a Tauc-Lorentz oscillator. The Tauc-Lorentz model has been used to account for absorption due to interband transitions and extract the optical constants of several doped semiconductors [41–43] including doped CdO films and nanoparticles [33,44]. The imaginary part of the dielectric function is given as:

$$\epsilon''_{TL}(\omega) = \frac{A_{TL}\omega_n C(\omega - \omega_T)^2}{(\omega^2 - \omega_n^2)^2 + \omega^2 C^2} \frac{\Theta(\omega - \omega_T)}{\omega}. \quad (2)$$

Here, A_{TL} , C , ω_n , and ω_T are fit parameters corresponding to the amplitude, broadening, center frequency and Tauc optical gap frequency, respectively. These parameters are provided in the Supplemental Material for all of the In:CdO films

in this study [39]. ω is the photon frequency and the Heaviside function $[\Theta(\omega - \omega_T)]$ is equal to zero for $\omega < \omega_T$ and one for $\omega > \omega_T$. Knowing the imaginary dielectric function, the real part can be calculated using the Kramers-Kronig relation [45]:

$$\epsilon'_{TL}(\omega) = \epsilon_{\infty,TL} + \frac{2}{\pi} P \int_{\omega_T}^{\infty} \frac{\xi \epsilon''(\xi)}{\xi^2 - \omega^2} d\xi. \quad (3)$$

The high-frequency permittivity ($\epsilon_{\infty,TL}$) describes the contribution to the real dielectric function well above the band gap and P indicates that the Cauchy principal value of the integral is to be taken.

From the ellipsometric spectra provided in Fig. 1, it is possible to extract the real and imaginary parts of the dielectric function. This procedure was performed for three films featuring carrier densities (Hall mobilities) of $6.6 \times 10^{19} \text{ cm}^{-3}$ ($426 \text{ cm}^2/\text{Vs}$), $1.4 \times 10^{20} \text{ cm}^{-3}$ ($389 \text{ cm}^2/\text{Vs}$), and $4.1 \times 10^{20} \text{ cm}^{-3}$ ($312 \text{ cm}^2/\text{Vs}$). The corresponding real and imaginary parts of the dielectric functions from $15000\text{--}30000 \text{ cm}^{-1}$ ($0.667\text{--}0.333 \mu\text{m}$) are provided in Fig. 2(a). The central energy of the absorption features corresponds to the CdO conduction band edge, which is observed to blue shift with increased carrier density due to the donor behavior of In dopants in CdO. As the carrier density increases the conduction band electron population is elevated which subsequently raises the Fermi energy, consistent with the Moss-Burstein effect [46,47]. The resultant E_g values of the CdO films are shown in Fig. 2(b) along with the previously reported values by Liu *et al.* [33] provided for comparison, illustrating that this observed effect is general to CdO films independent of growth method. The optical band-gap values were determined by first calculating the extinction coefficient (κ) from the extracted dielectric functions. The absorption coefficient ($\alpha = \frac{4\pi\kappa}{\lambda}$) can then be calculated and E_g approximated by extrapolating α^2 to zero. Plots of α^2 vs. photon energy are provided in the Supplemental Material [39]. The peak amplitude and broadening of the real dielectric function also follow a similar trend, implying increased absorption and loss around the band edge energy as the carrier density is increased.

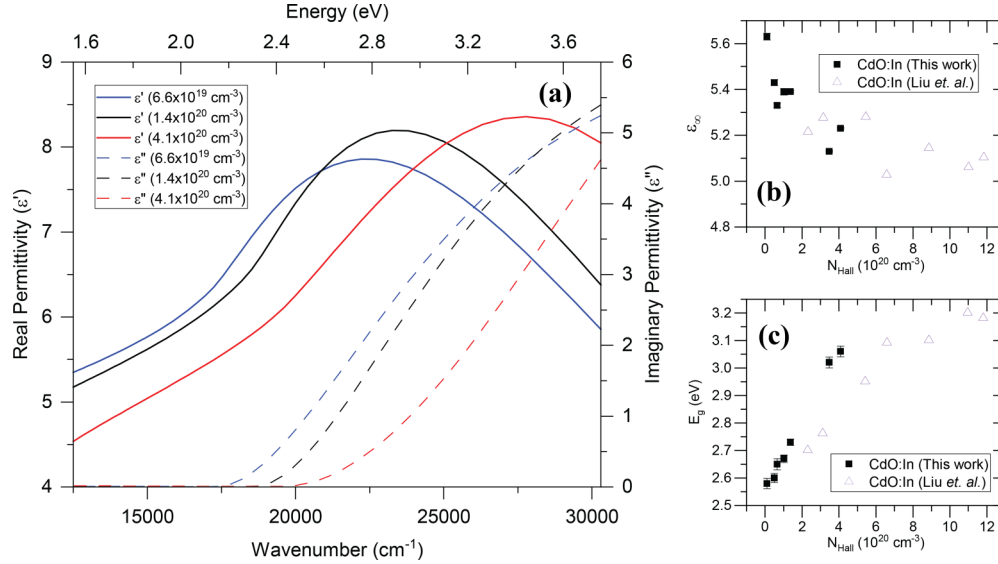


FIG. 2. (a) Real (solid) and imaginary (dashed) parts of the dielectric functions near the band-gap energy of three CdO thin films with differing carrier densities as labeled. Note the blue shift in the band-gap absorption with increasing carrier density. The optical band gap and high-frequency permittivity of In:CdO films as a function of carrier density are shown in (b) and (c), respectively. The uncertainty in the values, determined from the described fits are provided as error bars. Previously reported values from Liu *et al.* [33] are also shown in (b) and (c) for comparison.

These shifts in band edge energy and absorption impact the background polarizability of the lattice and therefore the extracted high-frequency permittivity (ϵ_∞) of the Drude function, which describes the dielectric function in the MIR. At low enough energies, sufficiently below the optical band gap, $\epsilon'_{TL}(\omega)$ takes the constant value of ϵ_∞ . As the band edge absorption shifts to higher energy with increasing N_d , the high-frequency permittivity is observed to decrease from 5.5–5.1 in our films [Fig. 2(c)]. This inverse relationship between the high-frequency permittivity and lowest-energy interband transition, known as Moss’s rule, has been well documented across many semiconductors [48]. High-frequency permittivity values were obtained by plotting real permittivity as a function of $(E^2 + \gamma^2)^{-1}$, where $E = \hbar\omega$ is photon energy and γ is Drude damping, which will be discussed in the following section, and determining the x intercept. Plots demonstrating the relationship between real permittivity and $(E^2 + \gamma^2)^{-1}$ as well as ϵ_∞ and E_g in these In:CdO films can be found in the Supplemental Material [39].

IV. EFFECTS OF FREE CARRIERS ON NEAR- TO FAR-INFRARED DIELECTRIC FUNCTION

While the residual polarizability from interband transitions dictates the scaling of the real part of the dielectric function within the IR, for CdO and other TCOs, this spectral range is dominated by free-carrier effects (due to the low, FIR energies of optic phonons in CdO, their influence upon the dielectric function will be discussed in the next section). The influence of free carriers can be modeled using the Drude formalism:

$$\epsilon_{\text{Drude}}(\omega) = -\frac{A_D}{\omega^2 + i\gamma\omega}. \quad (4)$$

The Drude model has been employed in the past to model the NIR-MIR complex dielectric functions of several other

highly doped semiconductors [49,50], as well as most metals [51,52]. In Eq. (4), A_D is expressed as $A_D = \epsilon_\infty\omega_p^2$. As is stated above, ϵ_∞ results from the background polarizability of the lattice due to interband transitions and was found to range from 5.1–5.6 [33]. Combining the real part of Eq. (4) with Eq. (3) results in the expression $\epsilon'_{TL}(\omega) + \epsilon'_{\text{Drude}}(\omega) = \epsilon'_{TL}(\omega) - \frac{A_D}{\omega^2 + \gamma^2}$. However, at energies significantly below the band edge absorption ϵ_∞ takes the place of $\epsilon'_{TL}(\omega)$. The imaginary part is driven by the free-carrier damping (γ), which is inversely related to the corresponding scattering lifetime. The plasma frequency $\omega_p = \sqrt{N_d e^2 / m^* \epsilon_\infty \epsilon_0}$ increases with the square root of the electron carrier density $\sqrt{N_d}$, with ϵ_0 and m^* representing the permittivity of free space and effective mass, respectively. The $\sqrt{N_d}$ scaling of ω_p can be discerned from the experimentally obtained values of ω_p in Fig. 3(a). From the dielectric functions provided in Fig. 4(a), we extracted corresponding ω_p of 2584 cm⁻¹ (6.6×10^{19} cm⁻³), 3680 cm⁻¹ (1.4×10^{20} cm⁻³), and 5215 cm⁻¹ (4.1×10^{20} cm⁻³), respectively. The values of ω_p for the other CdO films in this study are provided in the Supplemental Material and reported in Fig. 3(a) [39]. The relative rate of this scaling is dictated by the effective mass (m^*), which, for In:CdO, ranges from 0.11–0.26 m_0 for $N_d \sim 1 \times 10^{19}$ – 4×10^{20} cm⁻³, consistent with the nonparabolic conduction band model [53,54].

$$m^* = m_o^* \sqrt{1 + 2C \frac{\hbar^2}{m_o^*} (3\pi^2 N_d)^{2/3}}. \quad (5)$$

Here m_o^* is the effective mass at the base of the conduction band, C is a nonparabolicity fitting parameter, and N_d is assumed to be the carrier density measured in Hall effect measurements, N_{Hall} . Electron mobility was also determined through Hall effect measurements (μ_{Hall}). These values differ from optical mobility (μ_{opt}) values that were extracted

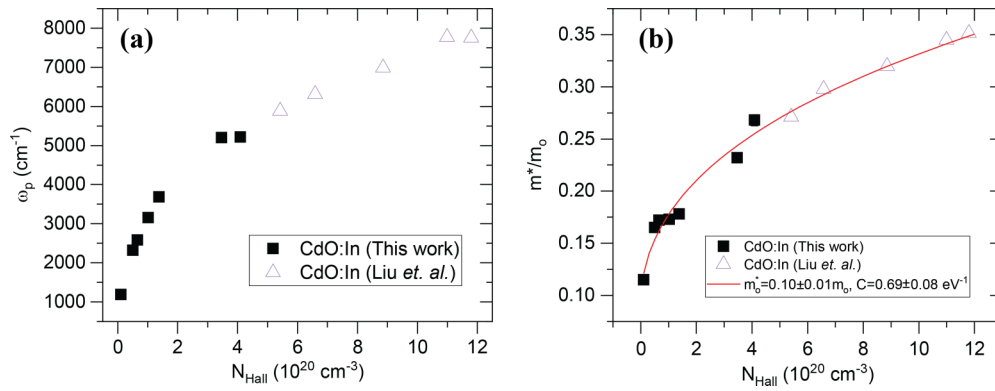


FIG. 3. (a) Plasma frequency ω_p and (b) effective mass m^* of doped CdO films as a function of carrier density. Previously reported values for both ω_p and m^* from Liu *et al.* [33] are also shown for comparison. A fit to the data using Eq. (5) is also provided (red curve).

through ellipsometric fitting. Optical mobility values are provided in the Supplemental Material along with a discussion of the discrepancies between Hall (μ_{Hall}) and optical mobility (μ_{opt}) [39]. Note that Fig. 3(b) includes the effective mass values for two sample sets: high-quality HiPIMS CdO films (black squares) and highly doped, polycrystalline films grown using MBE (purple triangles). Interestingly, our reported values of m^* in Fig. 3(b) demonstrate excellent continuity with these samples reported in previous work [33], illustrating that the growth quality appears to have little to no effect on the carrier-density-dependent effective mass of In:CdO. Effective mass has also been shown to be independent of crystallinity in other high-mobility TCOs, such as H : In₂O₃ [55]. We provide a fit to the combined m^* data, resulting in fitting parameter values of $C = 0.69 \pm 0.08 \text{ eV}^{-1}$, and $m_o^* = 0.10 \pm 0.01 m_o$. The excellent agreement across sample sets and two orders of magnitude in carrier density justifies the use of this fit for approximating the effective mass of In:CdO with great accuracy. This can be compared to the fit provided in Liu *et al.*, which resulted in $C = 0.49 \pm 0.19 \text{ eV}^{-1}$ and $m_o^* = 0.13 \pm 0.03 m_o$ for highly doped films alone ($N_d > 5 \times 10^{20} \text{ cm}^{-3}$) [33,56].

From Eq. (4), it is clear that the free carrier damping rate, defined as $\gamma = \frac{e}{\mu_{\text{opt}} m^*}$, is directly related to the imaginary part of the permittivity and therefore provides a convenient figure of merit for determining loss in polaritonic materials [57–59].

Using the extracted values of m^* and optical mobility (μ_{opt}), the damping rate was calculated for each film as a function of carrier density and is reported in Fig. 4(b). As was stated previously, μ (both optical and Hall values) is observed to increase in CdO up to $N_d \sim 5 \times 10^{19} \text{ cm}^{-3}$, however, CdO maintains consistently high electron mobilities even at carrier densities exceeding this value. Thus, the resulting low damping rates are shown to decrease over a broad range of carrier densities (and therefore, plasma frequencies), even in the region of decreasing electron mobility.

As these excellent CdO transport properties are widely beneficial for a variety of nanophotonic applications including chemical sensing [24,60], narrow-band thermal emitters [30], and nonlinear optics [61], quantifying the loss and comparing to state-of-the-art polaritonic materials is of distinct interest. A more insightful FOM can be found in the modal quality (Q) factor, which relates the energy stored to the energy dissipation rate within confined cavities. The Q factor is widely implemented in photonic resonators and can be predicted from the extracted dielectric function as [57]:

$$Q = \frac{\omega \frac{d\epsilon'}{d\omega}}{2\epsilon''}. \quad (6)$$

From this expression it can be seen that the Q factor for a localized SPP is inversely proportional to the imaginary part

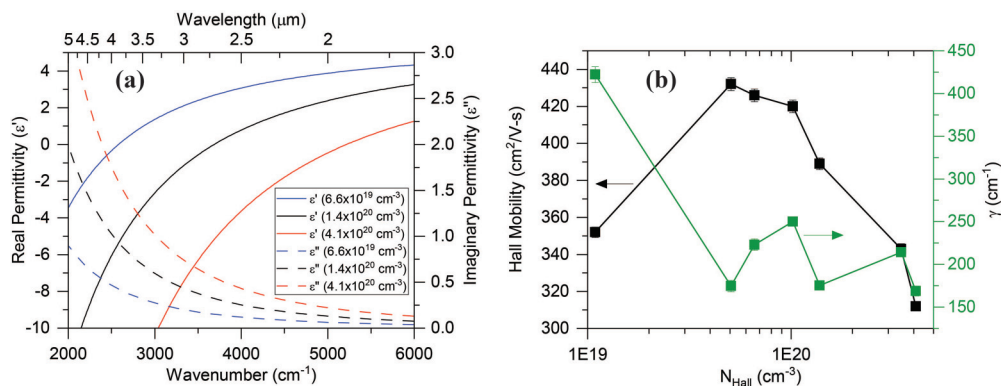


FIG. 4. (a) Real and imaginary dielectric function near the plasma frequency of three CdO thin films with differing carrier densities. The dielectric functions were derived from WVASE fitting of spectroscopic ellipsometry data. (b) Hall electron mobility and carrier damping (γ) as a function of carrier density in In:CdO films.

TABLE I. Comparison of optoelectronic properties of TCOs used in MIR plasmonics.

Material	Effective Mass $[m^*/m_o]$	N_d for $\lambda_p = 1.55 \mu\text{m}$ $[\times 10^{20} \text{cm}^{-3}]$	Carrier Mobility $[\text{cm}^2/\text{V} - \text{s}]$	$\text{Im}(\epsilon)$ at [$\text{Re}(\epsilon) = -2$] for Film of N_d in Column 3	Q eq. (6) at [$\text{Re}(\epsilon) = -2$] for Film of N_d in Column 3	Propagating FOM (FOM $\approx \frac{\omega_p}{\gamma}$) for Film of N_d in Column 3
ITO [73]	0.38	6.76	36	0.88	6.5	8.5
Ga:ZnO [74]	0.38	6.79	30.96	0.79	7.3	7.3
Al:ZnO [75]	0.38	6.75	47.6	0.59	9.5	11.2
H:In ₂ O ₃ [55]	0.28	5.46	118	0.37	18	22
In:CdO	0.27	5.36	285	0.20	24	48

of the dielectric function, while it is directly proportional to the frequency dispersion of the real part. Thus, to achieve high Q , the material losses must be low and/or the rate of change in the dielectric constants must be high. While Q factors in excess of 100 are routinely observed in surface phonon polariton resonators [24,58,62–64], the much slower dispersion of plasmonic materials, coupled with the faster scattering of free carriers with respect to optical phonons [65,66], naturally limits plasmonic cavities to values below 44, with typical values falling below 20 [67]. However, as the rate of dispersion does not vary significantly between plasmonic materials (thanks to the Drude model), it is the imaginary part of the dielectric function that predominantly determines Q for such materials. Therefore, considering a spherical resonator allows for an insightful comparison between materials: an analytical solution exists for the Mie scattering from such a structure, with resonance occurring at the Fröhlich condition [$\text{Re}(\epsilon) = -2\epsilon_a$] [68]. Here, ϵ_a is the real part of the permittivity for the ambient environment, which for air will result in the polaritonic resonance condition occurring at $\text{Re}(\epsilon) = -2$. To our knowledge the highest reported Q factor for noble metal resonators in the MIR is 20–25, as demonstrated with hollow silver nanotubes on a silver backplane [69]. Thus, the Q factor for In:CdO at the Fröhlich condition, calculated here from the dielectric function to reach up to 24, is on par with that of noble metal resonators in the MIR and ~ 3 –4 times higher than other TCOs, such as AZO [70], ITO [71], and GZO [72]. This is demonstrated in Table I, which compares the optoelectronic properties of CdO to other TCOs for films doped to achieve $\lambda_p = 1.55 \mu\text{m}$. Note, the carrier mobility of CdO is an order of magnitude larger than that of other TCOs, resulting in significantly lower $\text{Im}(\epsilon)$ and enhanced Q factors.

While Eq. (6) provides the means to compare plasmonic materials over a broad spectral range, it is typically more instructive to normalize the spectral dispersion in Q to the real part of the permittivity to eliminate the inherent spectral shifts in ω_p between materials as a function of carrier density. This has been provided in Fig. 5, which shows the range of Q -factor values at the Fröhlich condition for In:CdO along with the corresponding values for three other TCOs: ITO (red) [73], Al-doped (AZO, purple) [75], and Ga-doped (GZO, light blue) zinc oxide [74] as a function of ω_p (from 1500–4500 cm^{-1}). The dielectric functions for each TCO were calculated using Eq. (4). For AZO, GZO, and ITO the effective mass was calculated using Eq. (5) and the corresponding values of m_o^* and C [49], whereas the value listed in Table I was used for H : In₂O₃. A constant value for the carrier

mobility (provided in Table I) was assumed for ITO, AZO, GZO, and H : In₂O₃ however for CdO the mobility values were interpolated using the data provided in Fig. 4(b). From Fig. 5, it is clear that consistent with the analysis of spherical particles, In:CdO is anticipated to exhibit Q factors that are at least ~ 4 times higher than other common TCOs across a broad range of permittivity values and thus nanostructure shapes and sizes. In practice, the assumption of constant mobilities with increasing carrier densities in the other TCOs is not realistic and presumably overestimates the Q factors possible at high carrier density values. Further, the values for In:CdO actually compare favorably to measured values for silver ($Q \sim 20$ –25 in MIR), which still represents the highest quality noble metal for plasmonic applications. In addition, due to the consistently high carrier mobility and rapidly increasing effective mass, the Q factor is actually found to increase at a much faster rate in CdO than for other TCOs at elevated doping levels. Increasing Q factors with doping density have been reported previously in LSPRs supported by In:CdO nanoparticles within the near infrared [44]. As was mentioned above, the increase in Q factor is a result of the value of $\text{Im}(\epsilon)$ at the Fröhlich condition, which diminishes

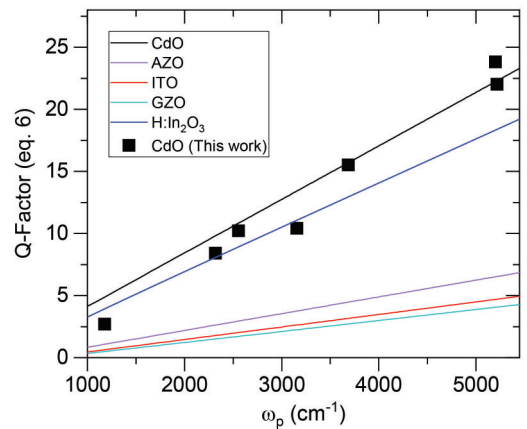


FIG. 5. Quality factor [Eq. (6)] calculated at the Fröhlich condition [$\text{Re}(\epsilon) = -2$] for several TCOs across a range of ω_p (and therefore N_d). The dielectric function for each material was calculated using the Drude model with the effective mass determined using Eq. (5). Values for m_o^* and C for other TCOs were found in literature [49,55]. Data points correspond to calculated Q -factor values from the extracted dielectric functions of the films in this study, demonstrating excellent agreement with the values calculated using the Drude model.

with increased N_d . Note, the imaginary permittivities at the condition $\text{Re}(\varepsilon) = -2$ for the CdO films with carrier densities of $6.6 \times 10^{19} \text{ cm}^{-3}$, $1.4 \times 10^{20} \text{ cm}^{-3}$, and $4.1 \times 10^{20} \text{ cm}^{-3}$ films [Fig. 4(a)] were determined to be $\text{Im}(\varepsilon) = 0.67, 0.45$, and 0.31 , respectively (see Table I in Supplemental Material for full set of data for each sample [39]). The measured Q -factor values are also provided in Fig. 5 for the films in this study, verifying this trend.

V. INFLUENCE OF OPTIC PHONONS ON CDO DIELECTRIC FUNCTION

As with other polar materials, the transverse-optic (TO) phonon of CdO is associated with a net dipole moment and is IR active. The restoring force of the ionic charge motion associated with the longitudinal-optic (LO) phonon lifts the degeneracy with the TO modes at the Γ point [76]. This increases the LO phonon frequency, resulting in a spectral band between these two optic phonon energies that is referred to as the Reststrahlen band. Within this band, polar materials are highly reflective, resulting from the charge screening of the oscillating polar crystal lattice. Just as light can couple to free charge oscillations in metals and doped semiconductors (SPPs), light can also couple to optic phonons in polar lattices. These excitations, known as surface phonon polaritons (SPhPs) are also of keen interest for IR nanophotonics [65,66,76,77]. This results from the real part of the permittivity becoming negative, with the ENZ condition occurring near the LO phonon frequency. In contrast to Drude response, for this so-called TOLO oscillator model the real part of the permittivity disperses rapidly, becoming progressively more negative with reducing frequency until the TO phonon frequency, at which point the sign of the permittivity is flipped, resulting in ultrahigh refractive indices due to the strong resonant absorption associated with the TO phonon [58,65,78,79]. For perspective, near the TO phonon in SiC, the index of refraction can exceed 20 (highest reported $n = 21.84$) [58,79–82]. This permittivity is typically defined by the so-called TOLO oscillator:

$$\varepsilon_{\text{TOLO}}(\omega) = \varepsilon_{\infty, \text{TOLO}} \left(\frac{\omega_{\text{LO}}^2 - \omega_{\text{TO}}^2}{\omega_{\text{TO}}^2 - \omega^2 - i\gamma\omega} \right), \quad (7)$$

where ω_{LO} and ω_{TO} correspond to the LO and TO phonon frequencies, respectively. The high-frequency permittivity, where here, $\varepsilon_{\infty, \text{TOLO}}$ defines the real part of the dielectric function at frequencies above the LO phonon frequency.

In undoped polar semiconductors and dielectrics, the TO phonon induces strong dispersion in the real part of the permittivity that dominates the IR dielectric function [83]. To examine the polar phonon contribution to the IR dielectric function, FIR reflectance measurements were performed at 60° angle of incidence on all three CdO films using a Bruker Vertex 70v FTIR spectrometer in tandem with a DLATGS detector. This was required as the optic phonons of CdO occur at frequencies beyond those sampled by the IR-VASE system ($>333 \text{ cm}^{-1}$). The strong absorptive nature of the TO phonon, which occurs at 266 cm^{-1} , is distinct in the reflectance spectra for the unintentionally doped CdO (red curve). The center frequency of this absorptive resonance agrees well with previously reported values for the CdO TO phonon using other

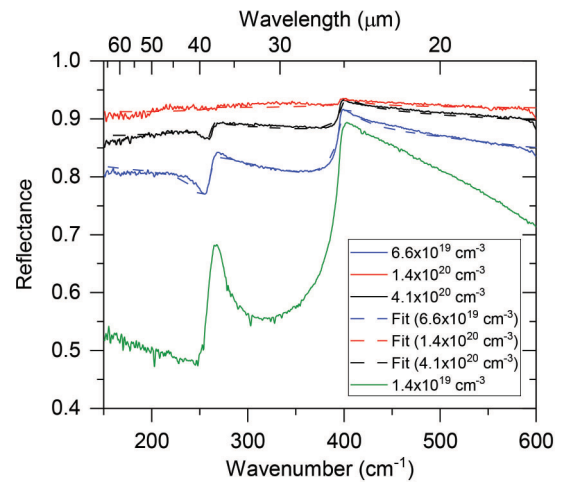


FIG. 6. Low-energy FTIR reflectance of four CdO films with varying levels of doping; unintentionally doped ($1.4 \times 10^{19} \text{ cm}^{-3}$), moderately doped ($6.6 \times 10^{19} \text{ cm}^{-3}$), and highly doped ($1.4 \times 10^{20} \text{ cm}^{-3}$ and $4.1 \times 10^{20} \text{ cm}^{-3}$) measured at an angle of incidence of 60° .

measurement techniques [84]. However, the relative intensity, with respect to the baseline reflectance, decreases as carrier density increases. This is demonstrated in the reflectance spectra in Fig. 6. Here the absorption resonance caused by the TO phonon is easily discernable in the unintentionally doped ($1.4 \times 10^{19} \text{ cm}^{-3}$) and low-doped ($6.6 \times 10^{19} \text{ cm}^{-3}$) CdO films, but is not observable in the higher carrier density ($1.4 \times 10^{20} \text{ cm}^{-3}$ and $4.1 \times 10^{20} \text{ cm}^{-3}$) films. This is consistent with the concept of the free-carrier contribution dominating the dielectric function with increased carrier density, where the higher carrier densities result in the real part of the dielectric function exhibiting larger negative values at the TO phonon frequency, thereby screening out the otherwise strong phonon absorption. This results in the reflection spectra flattening in the spectral region near the TO phonon, as shown in Fig. 6. The high reflectance above $\sim 400 \text{ cm}^{-1}$ is induced by optic phonons in the MgO substrate. Modeling the Lorentzian line shape of the TO phonon absorption observed in Fig. 6 using the TOLO formalism [Eq. (8)] enables the extraction of the spectral position and damping (phonon scattering rate) of the TO phonon within the various films. However, to perform this fitting, three of the four key values dictating the Lyddane-Sachs-Teller relationship must be known, with the fourth derived from this relation [76]. As for even the unintentionally doped CdO films there exists sufficient free carriers to preclude the observation of a distinct, highly reflective Reststrahlen band, a previously reported value for the LO phonon frequency from IR absorption measurements was employed as a starting value in the fitting process [85], while the TO phonon and damping were derived from the reflectance spectra, and the high-frequency permittivity extracted from the prior Drude fits.

From the above-referenced data, the phonon contribution to the FIR dielectric function can be derived, which are provided in Fig. 7(a) for the three films originally introduced in Figs. 2 and 4. A Lorentzian line shape can clearly be observed in the imaginary part of the dielectric function for all samples, regardless of N_d . However, the scaling of the ω_p

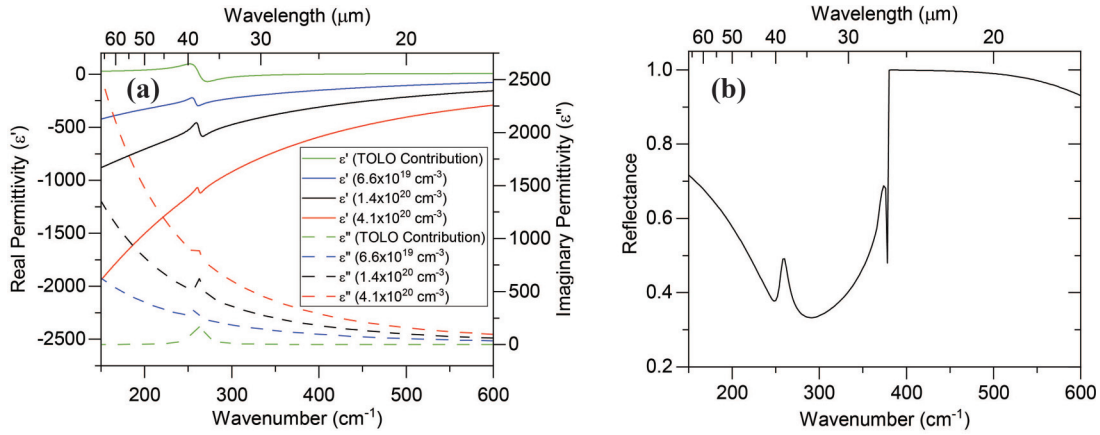


FIG. 7. Far-IR dielectric functions for (a) three CdO films with varying levels of doping as well as the isolated TOLO contribution (Drude and Tauc-Lorentz oscillators turned off). (b) Transfer-matrix-method reflectance simulation of a 200 nm CdO film with the TOLO-isolated dielectric function from (a) on an MgO substrate.

due to free carriers is evident in the FIR, resulting in a more negative real part and larger imaginary part of the permittivity with increased carrier density. The TOLO contribution to the dielectric function in the absence of free-carrier and band-gap effects is also displayed in Fig. 7(a). A transfer-matrix-method [86] calculation of the reflectance for a 200 nm CdO film using this TOLO-only dielectric function grown on a MgO substrate is presented in Fig. 7(b) and compares well with the FIR FTIR measurement of the unintentionally doped ($1.4 \times 10^{19} \text{ cm}^{-3}$) film shown in Fig. 6.

VI. COMBINED CDO DIELECTRIC FUNCTION

While we have presented the various contributions to the dielectric function of CdO within three distinct spectral ranges and described the salient features governing these effects separately, the combined spectral response is of course the primary goal of this work. Taking the three key contributions from Eqs. (2) and (3) (Tauc-Lorentz), (4) (Drude), and (7) (TOLO) together, the unified dielectric function can be described as follows:

$$\begin{aligned} \epsilon(\omega) &= \epsilon_{\text{TOLO}} + \epsilon_{\text{Drude}} + \epsilon_{\text{TL}} \\ &= \left(\epsilon_{\infty, \text{TL}} + \frac{2}{\pi} P \int_{\omega_T}^{\infty} \frac{\xi \epsilon''(\xi)}{\xi^2 - \omega^2} d\xi + i \frac{A \omega_n C (\omega - \omega_T)^2}{(\omega^2 - \omega_n^2)^2 + \omega^2 C^2} \frac{\Theta(\omega - \omega_T)}{\omega} - \frac{A_D}{\omega^2 + i\gamma\omega} \right) \left[\left(\frac{\omega_{\text{LO}}^2 - \omega_{\text{TO}}^2}{\omega_{\text{TO}}^2 - \omega^2 - i\gamma\omega} \right) \right]. \end{aligned} \quad (8)$$

Note that in this complete dielectric function, ϵ_{∞} in the Drude term, because the background polarizability of the lattice is represented by the band-gap contributions. The corresponding values for the various fitting parameters associated with each oscillator are provided in the Supplemental Material [39], while tabulated values may be downloaded from the Caldwell group’s website [87]. Using the above relations, with interpolated values derived from the films discussed here, the dielectric function of In:CdO extending from the visible to the FIR spectral range may be derived for arbitrary carrier density and mobility, which we expect will prove useful for accurate nanophotonic simulations that use In:CdO building blocks.

VII. CONCLUSION

With the ever-expanding interest into realizing advanced nanophotonic and optoelectronic concepts within the MIR spectral regime, the low optical losses and broad spectral tunability associated with CdO and other TCOs are of increasing interest. However, for the true potential of CdO for a variety of applications to be validated, predictive modeling of advanced optical or electrooptic components must be undertaken. This requires an accurate dielectric function,

which we have provided here over the spectral range from 150–33333 cm^{-1} (66–0.3 μm). A multioscillator model describing the near-UV-FIR complex dielectric function for doped CdO was extracted using spectroscopic ellipsometry, FIR FTIR spectroscopy, and dielectric function modeling using the WVASE program, implementing a least-squares fitting routine. Seven HiPIMS CdO films with varying levels of doping were characterized, giving insight into the role of free carriers not only upon the Drude term (through spectral shifting of the plasma frequency and effective mass and changes to carrier mobility), but also upon the band-gap-related interband transitions and in determining the relative role of the optic phonons at FIR frequencies. Using our extracted permittivity values, the prior assertions of CdO as one of the lowest loss MIR plasmonic materials for the 3–5 μm and 8–12 μm atmospheric windows were validated. This has implications for next generation IR sources [25], hot-carrier-based detectors and waveguides. Although the Drude term is the dominant feature of the extended CdO dielectric function, it is useful to include optic phonons and interband transitions into the model to further explain the ellipsometric line shapes at low and high frequencies, respectively, and to provide context as to the origin of the background permittivity outside of the

spectral range of these resonant modes. The model of the VASE data resulted in highly accurate fits, with the analysis presented here aiding in the demonstration of CdO-enabled next-generation nanophotonic and optoelectronic devices, while also providing an underlying physical description of the key properties dictating the dielectric response.

ACKNOWLEDGMENTS

We gratefully acknowledge support for this work by NSF Grant CHE-1507947, by Army Research Office Grants W911NF-16-1-0406 and W911NF-16-1-0037, and by Office

of Naval Research Grant N00014-18-12107. J.R.N, T.G.F. and J.D.C. both acknowledge support from Vanderbilt School of Engineering through the latter's start-up funding package. The work was performed, in part, at the Center for Integrated Nanotechnologies, an Office of Science User Facility operated for the US Department of Energy (DOE) Office of Science. Sandia National Laboratories is a multiprogram laboratory managed and operated by Sandia Corporation, a wholly owned subsidiary of Honeywell International Inc., for the U.S. Department of Energy's National Nuclear Security Administration under Contract DENA0003525.

-
- [1] T. Minami, *Semicond. Sci. Technol.* **20**, S35 (2005).
- [2] G. J. Exarhos and X. D. Zhou, *Thin Solid Films* **515**, 7025 (2007).
- [3] E. Sachet, C. T. Shelton, J. S. Harris, B. E. Gaddy, D. L. Irving, S. Curtarolo, B. F. Donovan, P. E. Hopkins, P. A. Sharma, A. L. Sharma, J. Ihlefeld, S. Franzen, and J. P. Maria, *Nature Mater.* **14**, 414 (2015).
- [4] A. Boltasseva and H. A. Atwater, *Science* **331**, 290 (2011).
- [5] K. Bädeker, *Ann. Phys. (N.Y.)* **327**, 749 (1907).
- [6] A. Wang, J. R. Babcock, N. L. Edleman, A. W. Metz, M. A. Lane, R. Asahi, V. P. Dravid, C. R. Kannewurf, A. J. Freeman, and T. J. Marks, *Proc. Natl. Acad. Sci.* **98**, 7113 (2002).
- [7] K. P. Kelley, E. Sachet, C. T. Shelton, and J.-P. Maria, *APL Mater.* **5**, 076105 (2017).
- [8] E. L. Runnerstrom, K. P. Kelley, E. Sachet, C. T. Shelton, and J. P. Maria, *ACS Photon.* **4**, 1885 (2017).
- [9] J. T. Gudmundsson, N. Brenning, D. Lundin, and U. Helmerson, *J. Vac. Sci. Technol. A* **30**, 030801 (2012).
- [10] A. Anders, *J. Appl. Phys.* **121**, 171101 (2017).
- [11] E. M. Larsson, J. Alegret, M. Käll, and D. S. Sutherland, *Nano Lett.* **7**, 1256 (2007).
- [12] L. Bo, N. Claes, and L. Ingemar, *Sens. Actuators* **4**, 299 (1983).
- [13] J. Cleary, R. Peale, D. Shelton, G. Boreman, R. Soref, and W. Buchwald, *MRS Proc.* **1133**, 1133 (2008).
- [14] K. H. Rieder, S. Nie, and S. R. Emory, *Probing Single Molecules and Single Nanoparticles by Surface-Enhanced Raman Scattering Downloaded From*, (Springer, Berlin, 1994).
- [15] J. D. Caldwell, O. Glembocki, F. J. Bezares, N. D. Bassim, R. W. Rendell, M. Feygelson, M. Ukaegbu, R. Kasica, L. Shirey, and C. Hosten, *ACS Nano* **5**, 4046 (2011).
- [16] J. D. Caldwell, O. J. Glembocki, F. J. Bezares, M. I. Kariniemi, J. T. Niinistö, T. T. Hatanpää, R. W. Rendell, M. Ukaegbu, M. K. Ritala, S. M. Prokes, C. M. Hosten, M. A. Leskelä, and R. Kasica, *Opt. Express* **19**, 26056 (2011).
- [17] R. Adato, A. A. Yanik, J. J. Amsden, D. L. Kaplan, F. G. Omenetto, M. K. Hong, S. Erramilli, and H. Altug, *Proc. Natl. Acad. Sci.* **106**, 19227 (2009).
- [18] D. Yoo, D. A. Mohr, F. Vidal-Codina, A. John-Herpin, M. Jo, S. Kim, J. Matson, J. D. Caldwell, H. Jeon, N. C. Nguyen, L. Martin-Moreno, J. Peraire, H. Altug, and S. H. Oh, *Nano Lett.* **18**, 1930 (2018).
- [19] R. Adato and H. Altug, *Nature Commun.* **4**, 2154 (2013).
- [20] X. Ni, N. K. Emani, A. V. Kildishev, A. Boltasseva, and V. M. Shalaev, *Science* **335**, 427 (2012).
- [21] F. Aieta, P. Genevet, M. A. Kats, N. Yu, R. Blanchard, Z. Gaburro, and F. Capasso, *Nano Lett.* **12**, 4932 (2012).
- [22] F. Capasso, P. Genevet, J.-P. Tetienne, M. A. Kats, Z. Gaburro, N. Yu, and F. Aieta, *Science* **334**, 333 (2011).
- [23] G. V. Naik, V. M. Shalaev, and A. Boltasseva, *Adv. Mater.* **25**, 3264 (2013).
- [24] M. Autore, P. Li, I. Dolado, F. J. Alfaro-Mozaz, R. Esteban, A. Atxabal, F. Casanova, L. E. Hueso, P. Alonso-González, J. Aizpurua, A. Y. Nikitin, S. Vélez, and R. Hillenbrand, *Light Sci. Appl.* **7**, 17172 (2018).
- [25] T. Wang, P. Li, D. N. Chigrin, A. J. Giles, F. J. Bezares, O. J. Glembocki, J. D. Caldwell, and T. Taubner, *ACS Photonics* **4**, 1753 (2017).
- [26] Y. Gu, X. Li, J. Chen, and H. Zeng, *Opt. Express* **24**, 29908 (2016).
- [27] C. Sönnichsen, T. Franzl, T. Wilk, G. von Plessen, J. Feldmann, O. Wilson, and P. Mulvaney, *Phys. Rev. Lett.* **88**, 077402 (2002).
- [28] S. Vassant, J.-P. Hugonin, F. Marquier, and J.-J. Greffet, *Opt. Express* **20**, 23971 (2012).
- [29] S. Campione, I. Brener, and F. Marquier, *Phys. Rev. B* **91**, 121408 (2015).
- [30] K. P. Kelley, E. L. Runnerstrom, E. Sachet, C. T. Shelton, E. D. Grimley, A. Klump, J. M. Lebeau, Z. Sitar, J. Y. Suen, W. J. Padilla, and J.-P. Maria, *ACS Photonics* **6**, 1139 (2019).
- [31] E. L. Runnerstrom, K. P. Kelley, T. G. Folland, J. R. Nolen, N. Engheta, J. D. Caldwell, and J. P. Maria, *Nano Lett.* **19**, 948 (2019).
- [32] N. C. Passler, C. R. Gubbin, T. G. Folland, I. Razdolski, D. S. Katzer, D. F. Storm, M. Wolf, S. De Liberato, J. D. Caldwell, and A. Paarmann, *Nano Lett.* **18**, 4285 (2018).
- [33] C. P. Liu, Y. Foo, M. Kamruzzaman, C. Y. Ho, J. A. Zapien, W. Zhu, Y. J. Li, W. Walukiewicz, and K. M. Yu, *Phys. Rev. Appl.* **6**, 064018 (2016).
- [34] M. Burbano, D. O. Scanlon, and G. W. Watson, *J. Am. Chem. Soc.* **133**, 15065 (2011).
- [35] C. M. Herzinger, B. Johs, W. A. Mcgahan, J. A. Woollam, and W. Paulson, *J. Appl. Phys.* **83**, 3323 (1998).
- [36] J. Y. Yang, W. J. Zhang, L. H. Liu, J. Qiu, K. Wang, and J. Y. Tan, *J. Chem. Phys.* **141**, 104703 (2014).
- [37] D. T. Speaks, M. A. Mayer, K. M. Yu, S. S. Mao, E. E. Haller, and W. Walukiewicz, *J. Appl. Phys.* **107**, 113706 (2010).
- [38] P. D. C. King, T. D. Veal, C. F. McConville, J. Zúñiga-Pérez, V. Muñoz-Sanjose, M. Hopkinson, E. D. L. Rienks, M. F. Jensen, and P. Hofmann, *Phys. Rev. Lett.* **104**, 256803 (2010).

- [39] See Supplemental Material at <http://link.aps.org/supplemental/10.1103/PhysRevMaterials.4.025202> for CdO film properties, ellipsometric fit parameters and detailed fitting procedure.
- [40] J. W. Cleary, E. M. Smith, K. D. Leedy, G. Grzybowski, and J. Guo, *Opt. Mater. Express* **8**, 1231 (2018).
- [41] G. E. Jellison Jr., V. I. Merkulov, A. A. Poretzky, D. B. Geohegan, G. Eresa, D. H. Lowndes, and J. B. Caughman, *Thin Solid Films* **377-378**, 68 (2000).
- [42] D. V. Likhachev, N. Malkova, and L. Poslavsky, *Thin Solid Films* **589**, 844 (2015).
- [43] J. Budai, I. Hanyecz, E. Szilágyi, and Z. Tóth, *Thin Solid Films* **519**, 2985 (2011).
- [44] T. R. Gordon, T. Paik, D. R. Klein, G. V. Naik, H. Caglayan, A. Boltasseva, and C. B. Murray, *Nano Lett.* **13**, 2857 (2013).
- [45] G. E. Jellison and F. A. Modine, *Appl. Phys. Lett.* **69**, 371 (1996).
- [46] E. Burstein, *Phys. Rev.* **93**, 632 (1954).
- [47] T. S. Moss, *Proc. Phys. Soc. B* **67**, 775 (1954).
- [48] T. S. Moss, *Phys. Status Solidi* **131**, 415 (1985).
- [49] H. Fujiwara and M. Kondo, *Phys. Rev. B* **71**, 075109 (2005).
- [50] J. Ederth, P. Heszler, A. Hultåker, G. A. Niklasson, and C. G. Granqvist, *Thin Solid Films* **445**, 199 (2003).
- [51] P. B. Johnson and R. W. Christy, *Phys. Rev. B* **6**, 4370 (1972).
- [52] E. Palik, *Handbook of Optical Constants of Solids* (Elsevier, Amsterdam, 1985).
- [53] T. Pisarkiewicz, K. Zakrzewska, and E. Leja, *Thin Solid Films* **174**, 217 (1989).
- [54] T. Pisarkiewicz and A. Kolodziej, *Phys. Status Solidi* **158**, K5 (1990).
- [55] T. Koida, M. Kondo, K. Tsutsumi, A. Sakaguchi, M. Suzuki, and H. Fujiwara, *J. Appl. Phys.* **107**, 033514 (2010).
- [56] R. J. Mendelsberg, Y. Zhu, and A. Anders, *J. Phys. D: Appl. Phys.* **45**, 425302 (2012).
- [57] F. Wang and Y.R. Shen, *Phys. Rev. Lett.* **97**, 206806 (2006).
- [58] J. D. Caldwell, O. J. Glembocki, Y. Francescato, N. Sharac, V. Giannini, F. J. Bezares, J. P. Long, J. C. Owrutsky, I. Vurgaftman, J. G. Tischler, V. D. Wheeler, N. D. Bassim, L. M. Shirey, R. Kasica, and S. A. Maier, *Nano Lett.* **13**, 3690 (2013).
- [59] J. B. Khurgin and G. Sun, *Appl. Phys. Lett.* **96**, 181102 (2010).
- [60] A. Agrawal, A. Singh, S. Yazdi, A. Singh, G. K. Ong, K. Bustillo, R. W. Johns, E. Ringe, and D. J. Milliron, *Nano Lett.* **17**, 2611 (2017).
- [61] Y. Yang, K. Kelley, E. Sachet, S. Campione, T. S. Luk, J. P. Maria, M. B. Sinclair, and I. Brener, *Nature Photonics* **11**, 390 (2017).
- [62] Y. Chen, Y. Francescato, J. D. Caldwell, V. Giannini, T. W. W. Ma, O. J. Glembocki, F. J. Bezares, T. Taubner, R. Kasica, M. Hong, and S. A. Maier, *ACS Photonics* **1**, 718 (2014).
- [63] J. D. Caldwell, A. V. Kretinin, Y. Chen, V. Giannini, M. M. Fogler, Y. Francescato, C. T. Ellis, J. G. Tischler, C. R. Woods, A. J. Giles, M. Hong, K. Watanabe, T. Taniguchi, S. A. Maier, and K. S. Novoselov, *Nature Commun.* **5**, 5221 (2014).
- [64] M. Tamagnone, K. Chaudhary, A. Zhu, M. Meretska, J. Li, J. H. Edgar, A. Ambrosio, and F. Capasso, *arXiv:1905.02177*.
- [65] J. D. Caldwell, L. Lindsay, V. Giannini, I. Vurgaftman, T. L. Reinecke, S. A. Maier, and O. J. Glembocki, *Nanophotonics* **4**, 44 (2015).
- [66] S. Foteinopoulou, G. C. R. Devarapu, G. S. Subramania, S. Krishna, and D. Wasserman, *Phonon-Polaritons: Enabling Powerful Capabilities for Infrared Photonics* (DeGruyter, Berlin, 2019).
- [67] H. U. Yang, J. D'Archangel, M. L. Sundheimer, E. Tucker, G. D. Boreman, and M. B. Raschke, *Phys. Rev. B* **91**, 235137 (2015).
- [68] C. F. Bohren and D. R. Huffman, *Absorption and Scattering of Light by Small Particles*, 6th ed. (Wiley, New York, 1983).
- [69] M. Malerba, A. Alabastri, E. Miele, P. Zilio, M. Patrini, D. Bajoni, G. C. Messina, M. Dipalo, A. Toma, R. P. Zaccaria, and F. De Angelis, *Sci. Rep.* **5**, 16436 (2015).
- [70] S. Cornelius, M. Vinnichenko, N. Shevchenko, A. Rogozin, A. Kolitsch, and W. Möller, *Appl. Phys. Lett.* **94**, 042103 (2009).
- [71] Z. Chen, Y. Zhuo, W. Tu, Z. Li, X. Ma, Y. Pei, and G. Wang, *Opt. Express* **26**, 22123 (2018).
- [72] R. S. Ajimsha, A. K. Das, P. Misra, M. P. Joshi, L. M. Kukreja, R. Kumar, T. K. Sharma, and S. M. Oak, *J. Alloys Compd.* **638**, 55 (2015).
- [73] S. Ray, R. Banerjee, N. Basu, A. K. Batabyal, and A. K. Barua, *J. Appl. Phys.* **54**, 3497 (1983).
- [74] S. M. Park, T. Ikegami, and K. Ebihara, *Thin Solid Films* **513**, 90 (2006).
- [75] H. Agura, A. Suzuki, T. Matsushita, T. Aoki, and M. Okuda, *Thin Solid Films* **445**, 263 (2003).
- [76] S. Adachi, *Optical Properties of Crystalline and Amorphous Semiconductors: Materials and Fundamental Principles*, (Springer, New York, 1999).
- [77] F. Hillenbrand, R. Taubner, and T. Keilmann, *Nature (London)* **418**, 159 (2002).
- [78] A. Howes, J. R. Nolen, J. D. Caldwell, and J. Valentine, *Adv. Optical Mater.* 1901470 (2019), doi:[10.1002/adom.201901470](https://doi.org/10.1002/adom.201901470).
- [79] T. E. Tiwald, J. A. Woollam, S. Zollner, J. Christiansen, R. B. Gregory, T. Wetteroth, S. R. Wilson, and A. Powell, *Phys. Rev. B* **60**, 11464 (1999).
- [80] J. A. Schuller, R. Zia, T. Taubner, and M. L. Brongersma, *Phys. Rev. Lett.* **99**, 107401 (2007).
- [81] J. A. Schuller, T. Taubner, and M. L. Brongersma, *Nature Photonics* **3**, 658 (2009).
- [82] J. Kim, A. Dutta, G. V Naik, A. J. Giles, F. J. Bezares, C. T. Ellis, J. G. Tischler, A. M. Mahmoud, H. Caglayan, O. J. Glembocki, A. V Kildishev, J. D. Caldwell, A. Boltasseva, and N. Engheta, *Optica* **3**, 339 (2016).
- [83] M. Schubert, T. E. Tiwald, and C. M. Herzinger, *Phys. Rev. B* **61**, 8187 (2000).
- [84] R. Cuscó, J. Ibáñez, N. Domenech-Amador, L. Artús, J. Zúñiga-Pérez, and V. Muñoz-Sanjosé, *J. Appl. Phys.* **107**, 063519 (2010).
- [85] H. Finkenrath, N. Uhle, and W. Waidelich, *Solid State Commun.* **7**, 11 (1969).
- [86] N. C. Passler and A. Paarmann, *J. Opt. Soc. Am. B* **34**, 2128 (2017).
- [87] CdO dielectric functions can be found at: <https://my.vanderbilt.edu/caldwellgroup/dielectric-functions/>, 2019.

Correction: A typographical error in the value for C appearing after Eq. (5) has been fixed, with a related change to the key inside Fig. 3(b). The top axis in Fig. 2(a) contained an error and has been resolved.